

Role of Ti-Ru interaction in SrTi_{0.5}Ru_{0.5}O₃: Physical properties, x-ray spectroscopy, and cluster model calculations

E. B. Guedes,^{1,*} F. Abud,² H. P. Martins,¹ M. Abbate,¹ R. F. Jardim,² and R. J. O. Mossaneck^{1,†}

¹Departamento de Física, Universidade Federal do Paraná Caixa Postal 19044, 81531-990 Curitiba, Paraná, Brazil

²Instituto de Física, Universidade de São Paulo, Rua do Matão, 1371, 05508-090, São Paulo, Brazil



(Received 13 November 2018; revised manuscript received 6 July 2019; published 15 August 2019)

We have performed a systematic study of the physical properties and electronic structure of SrTiO₃, SrTi_{0.5}Ru_{0.5}O₃, and SrRuO₃. For the mixed compound, the temperature dependence of the magnetization is consistent with the occurrence of RuTi and TiRu defects. Despite being a semiconductor, the behavior of the electrical resistivity as a function of temperature is compatible with the emergence of small metallic regions richer in Ru concentration, a feature supported by the finite spectral weight at the Fermi level observed in the valence-band x-ray photoemission spectroscopy spectrum. The x-ray photoemission and absorption spectra of the SrTi_{0.5}Ru_{0.5}O₃ compound were simulated by double cluster model calculations, which include the TiO₆-RuO₆ interaction, and also by the linear combination of single cluster calculations for SrTiO₃ and SrRuO₃. The results indicate that the interaction between different octahedra may give rise to distinct peak characters, depending on the experimental spectrum being calculated. We argue that these effects are only captured with the explicit inclusion of the Ti-Ru interaction.

DOI: [10.1103/PhysRevB.100.075132](https://doi.org/10.1103/PhysRevB.100.075132)

I. INTRODUCTION

Transition-metal oxides are the center of many important discoveries in the condensed-matter field in the last decades, such as high- T_c superconductivity [1] and giant magnetoresistance [2]. The great interest in these materials is led not only by their myriad of intriguing physical properties but also by many underlying phase transitions, which can be induced by changes in temperature, pressure, chemical substitution, and doping [3]. In particular, ruthenium oxides form a unique family of compounds which regained attention after the discovery of superconductivity in Sr₂RuO₄ [4]. Other well-known examples are paramagnetic-to-ferromagnetic phase transition in Ca_{1-x}Sr_xRuO₃ [5,6], and the variety of phases in the Ruddlesden-Popper series Sr_{n+1}Ru_nO_{3n+1} [7,8].

More recently, the SrTi_{1-x}Ru_xO₃ (STRO) series was the subject of a number of studies regarding its structural, transport, and optical properties, as well as its electronic structure. On the $x = 0$ side of the series, bulk SrTiO₃ (STO) exhibits cubic structure at room temperature which can evolve to a tetragonal (110–65 K), orthorhombic, (55–35 K), and possibly a rhombohedral phase below 10 K [9]. It is a diamagnetic band insulator with a direct gap close to 3.2 eV [10].

On the $x = 1$ end of the phase diagram, SrRuO₃ (SRO) crystallizes in an orthorhombic distorted perovskite structure at room temperature [11], it is metallic [12], and it displays either Fermi-liquid [13] or bad metal [14,15] behavior, depending on the temperature range analyzed. Also, SrRuO₃ can be classified as an itinerant ferromagnetism with Curie

temperature $T_C \approx 160$ K and a magnetic moment of $\mu_{\text{eff}} \approx 1.60\mu_B/\text{f.u.}$ [16,17], being the only 4d transition-metal (TM) oxide to exhibit metallic and ferromagnetic properties on the same crystal phase.

The SrTi_{1-x}Ru_xO₃ series exhibits cubic structure for $x < 0.30$, tetragonal for $0.30 \leq x \leq 0.40$, and orthorhombic for $x > 0.40$. Electrical resistivity measurements indicate insulating behavior for $x \approx 0.0$ ($d\rho/dT > 0$). According to Kim et al., Ru doping in films of this series leads to different ground states, namely, disordered correlated insulator ($x \approx 0.2$), soft Coulomb gap insulator ($x \approx 0.4$), and Anderson insulator ($x \approx 0.5$). For $x \approx 0.7$ a metal-insulator transition (MIT) takes place, turning the system into a disordered metal and finally to a correlated metal for $x \approx 1.0$.

The electronic structure of the SrTi_{1-x}Ru_xO₃ series has been studied with x-ray photoemission and absorption spectroscopies, as well as density functional theory (DFT) calculations. Early works on polycrystalline STRO supported that the Ti 3d and Ru 4d bands should be decoupled, and suggested that the metal-insulator transition at $x_c \approx 0.35$ belongs to the universality class of percolation phase transitions [18]. Kim et al. performed photoemission and absorption measurements of SrTi_{1-x}Ru_xO₃ series and addressed the metal-insulator transition as being caused by correlation and disorder effects [19]. Band-structure calculations for STRO indicated that the metal-insulator phase transition could be related to the increase of correlation strength in the Ru site [20], while other *ab initio* studies suggested that the low-Ti side of the SrTi_{1-x}Ru_xO₃ series would exhibit a half-metallic phase [21]. More recently, studies on the effect of disorder in thin films of Sr₂TiRuO₆ supported the proposal that the 4d state connectivity between neighboring Ru atoms could strongly influence the electronic structure near the Fermi energy, and thus, the electronic properties of the compound [22].

*Present address: Swiss Light Source, Paul Scherrer Institut, CH-5232 Villigen, Switzerland; eduardo.bonini-guedes@psi.ch

†mossaneck@fisica.ufpr.br

We describe here the results of our studies of the physical properties and electronic structure of SrTiO₃, SrTi_{0.5}Ru_{0.5}O₃, and SrRuO₃ polycrystals. The x-ray diffraction suggests three different crystallographic phases for the three different samples, while the magnetization and electrical resistivity measurements suggest the occurrence of RuTi and TiRu defects, giving rise to small metallic regions richer in Ru concentration. The electronic structure was probed with x-ray photoemission and absorption, and interpreted by means of cluster model calculations. In particular, the spectra for the SrTi_{0.5}Ru_{0.5}O₃ compound were simulated by considering two approaches: (i) a double cluster model calculation taking into account the interaction between TiO₆ and RuO₆ octahedra, and (ii) weighting the results of a single cluster model for each end member of the series. This strategy allows us to address how the interaction between SrTiO₃ and SrRuO₃ clusters can affect the analysis of the electronic structure on SrTi_{0.5}Ru_{0.5}O₃. We show that the impact of the explicit inclusion of Ru-Ti interaction is dependent on the spectroscopic technique, and that although both approaches can describe the overall shape of the experimental data, the composition of the states forming each peak in the different spectra differs from one model to the other. We argue that both Ti-Ru disorder and electronic correlation are important ingredients for the description of the electronic structure of the SrTi_{1-x}Ru_xO₃ series close to $\approx 50\%$ substitution.

II. EXPERIMENTAL DETAILS

Polycrystalline samples of SrTi_{1-x}Ru_xO₃ ($x = 0, 0.5, \text{ and } 1$) were synthesized by the solid-state reaction method. Phase identification and unit-cell parameters were determined by refining powder x-ray diffraction patterns [23]. Magnetization $M(T)$ measurements, taken on parallelepiped-shaped samples, were performed in a commercial superconducting quantum interference device magnetometer from Quantum Design in the temperature range between 5 and 300 K under zero-field-cooled (ZFC) and field-cooled (FC) conditions. Temperature dependence of the electrical resistivity $\rho(T)$ were conducted in small rectangular pieces with the standard four-probe method and performed in a commercial Quantum Design PPMS Dynacool apparatus in the temperature range of $2 \text{ K} \leq T \leq 300 \text{ K}$.

X-ray spectroscopy

The spectroscopic measurements were carried out at the Laboratório Nacional de Luz Síncrotron (LNLS), Campinas, Brazil. The x-ray photoemission spectroscopy (XPS) measurements were performed at the SXS beamline [24], using a photon energy of 2830 eV. At these photon energies, the photoelectron escape depth is around 30 Å [25], which makes the signal less surface sensitive than typical photoelectron spectroscopy measurements performed with lower photon energies. The overall energy resolution was about 0.3 eV. The Fermi level was calibrated using a clean Au foil. The O 1s x-ray absorption spectroscopy (XAS) was performed in the total electron yield mode at the PGM beamline. The energy resolution was approximately 0.1 eV. The photon energy scale was calibrated using known peak positions of reference sam-

ples. The samples were scraped with a diamond file to remove any surface contamination. All spectra were acquired at room temperature with the base pressure around 3×10^{-9} mbar.

III. CALCULATION DETAILS

A. Single cluster model

The cluster model consists of solving a regular TMO₆ octahedron with a symmetry-adapted configuration interaction method [3,26]. Beyond the purely ionic configuration d^n of the TM, the N-electrons ground state (GS) $|\Psi_{\text{GS}}\rangle$ is expanded in the $d^{n+1}\underline{L}$, $d^{n+2}\underline{L}^2$, etc., configurations, where \underline{L} denotes a hole at the ligand (O $2p$) band. The Hamiltonian, obtained in a base of these configurations, includes the on-site Coulomb repulsion U , the O $2p$ -TM charge transfer energy Δ , and the $T_\sigma = \sqrt{3}pd\sigma$ and $T_\pi = 2pd\pi$ transfer integrals, in octahedral symmetry [27]. Further, a core hole potential $Q = U/0.83$ is included in core-level calculations [28]. The multiplet splitting is given in terms of the crystal-field splitting $10Dq$ and the intra-atomic exchange J .

In addition to the usual ligand screening, a nonlocal screening from a coherent band was included for metallic fluctuations in the Ru octahedra [29,30]. This band is composed of delocalized Ru $4d$ states at the Fermi level, and possesses Ru character with only minority t_{2g} symmetry, which is in line with DFT calculations [20,21]. Therefore, the Ru site configurations also consider the $d^{n+1}\underline{C}$, $d^{n+2}\underline{L}\underline{C}$, $d^{n+2}\underline{C}^2$, etc., configurations, where \underline{C} denotes a hole at the coherent band. The extra parameters related to the coherent band are the charge-transfer energy Δ^* and the effective transfer integral T^* . It is worth noting that although SrTi_{0.5}Ru_{0.5}O₃ was reported as an insulator in recent studies [22,31], this type of fluctuation would be present in SRO patches in the sample which are not delocalized throughout the compound. This consideration is in line with the disorder dependence of the spectral weight close to the Fermi level in STRO thin films [22].

The corresponding core $|\Psi_{\text{CS}}\rangle$, removal $|\Psi_{\text{RS}}^{N-1}\rangle$, and addition $|\Psi_{\text{AS}}^{N+1}\rangle$ final states are obtained by either removing a core or valence electron, or by adding an electron to the ground state. All Hamiltonians are solved with exact diagonalization, and the spectra are then calculated using the sudden approximation,

$$A(\omega) = \sum_j |\langle \Psi_f^j | \hat{O} | \Psi_{\text{GS}} \rangle|^2 \delta[\omega \pm (E_f^j - E_{\text{GS}})],$$

where $|\Psi_{\text{GS}}\rangle$ represents the ground-state wave function, and $|\Psi_f^j\rangle$ denotes the j th eigenstate of final state f (which can be a core, removal, or addition state, depending on the experimental procedure) with energies E_{GS} and E_f^j , respectively. \hat{O} is the operator corresponding to each experimental technique, e.g., \hat{d}_{core} , which annihilates a core electron, for core-level photoemission spectroscopy. The resulting discrete transitions are convoluted with Lorentzian and Gaussian functions to account for lifetime broadening and experimental resolution.

B. Double cluster model

The double cluster model consists of solving two TMO₆ octahedra joined by the vertex, with distinct ionic d^m and

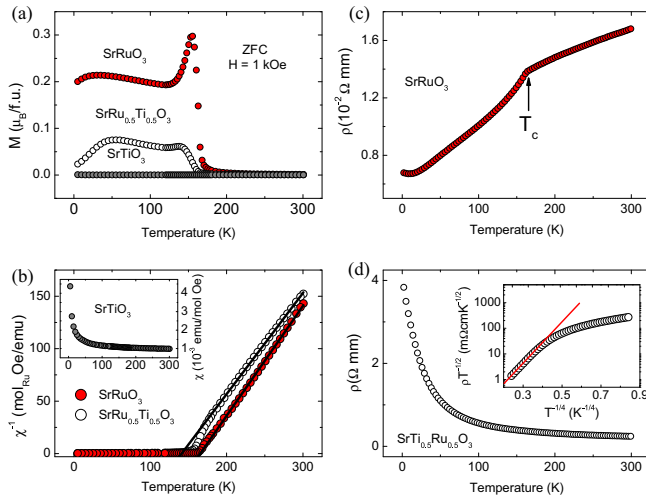


FIG. 1. (a) The temperature dependence of the (ZFC) magnetization of $\text{SrTi}_{1-x}\text{Ru}_x\text{O}_3$ samples. (b) Reciprocal magnetic susceptibility $\chi^{-1}(T)$ along with the Curie-Weiss fits in $T > T_C$ which are represented by continuous lines. The inset displays the paramagnetic behavior of SrTiO_3 . (c) Temperature dependence of the electrical resistivity $\rho(T)$ of the SrRuO_3 sample with metallic behavior. (d) Semiconducting behavior of the $\text{SrTi}_{0.5}\text{Ru}_{0.5}\text{O}_3$ compound. The inset exhibits the linear behavior of $\rho(T^{1/2})$ vs $T^{-1/4}$ data, as indicated by the continuous red line in the figure.

d^n configurations, which interact through the shared oxygen atom. The new basis configurations are obtained by the combination of both TM's basis, such as $d_{\text{Ti}}^{m+r} \underline{L}^{p+r} C^q d_{\text{Ru}}^{n+p+q}$, which includes the respective ligand/coherent fluctuations at each site. Also, the \hat{O} operators for the calculation of the spectral weight gain a TM index, e.g., $\hat{d}_{\text{core}}^{\text{Ti}}$, which annihilates a Ti core electron, etc. All other procedures remain the same as in the single cluster case. A similar double cluster model has recently been employed to study rare-earth nickelates [32].

Double cluster model calculations are much more computationally demanding than single cluster model calculations, which can usually be performed using a complete basis set including elements from the ionic d^n up to the $d^{10} \underline{L}^{10-n}$ configurations. Therefore, in all present calculations a maximum of four holes, ligand and coherent, were admitted. For consistency, the same maximum number of ligand holes were used in the single cluster calculations. The basis restriction provided an accuracy of 10^{-2} eV for the ground-state energy, which is enough to describe the energy scale of the interactions included in the model, as well as consistent with the experimental resolution.

IV. RESULTS

A. Magnetization

Figure 1(a) exhibits the temperature dependence of the magnetization $M(T)$ under an external applied magnetic field of $H = 1$ kOe in the ZFC mode. Ferromagnetic (FM) order is observed to occur in temperatures below $T_C \approx 160$ K in the SrRuO_3 compound, as it has been widely reported in this material [12]. The partial substitution of Ru ions by nonmagnetic Ti^{4+} in $\text{SrTi}_{0.5}\text{Ru}_{0.5}\text{O}_3$ weakens the FM order

of the Ru sublattice leading to both smaller values of $M(T)$ and a progressive decrease of $T_C \approx 45$ K, as suggested by the data. Weakening of the FM order in SrRuO_3 by nonmagnetic doping has also been observed previously [33,34] and reflects the gradual localization of the Ru $4d$ electrons with Ti substitution. The ruthenium effective magnetic moments μ_{eff} of SrRuO_3 and $\text{SrTi}_{0.5}\text{Ru}_{0.5}\text{O}_3$ were estimated from fittings of the Curie-Weiss law by using the temperature-dependent reciprocal magnetic susceptibility $\chi^{-1}(T)$, $T > T_C$, shown in Fig. 1(b). Besides of the good agreement between the obtained μ_{eff} values 1.44 and $1.38\mu_B$, respectively, the fitting results are close to the one reported for the localized magnetic moment per Ru^{4+} of around $1.5\mu_B$ [15], which is believed to deviate from the spin-only value due to hybridization with O $2p$ states [12,15]. This result further suggests that the oxidation state of the Ru ion and strong interaction with the ligand is preserved in the mixed compound.

The solid solution sample $\text{SrTi}_{0.5}\text{Ru}_{0.5}\text{O}_3$ also exhibited clear deviation from the Curie-Weiss law at temperatures below 160 K, and the establishment of long-range order at $T_C \approx 140$ K. Such a deviation of the Curie-Weiss behavior just below 160 K is consistent with the occurrence of regions within the material with short-range composition fluctuations in the vicinity of the stoichiometric composition $x = 0.5$. The occurrence of local composition fluctuations, being difficult to detect by XPS and XAS techniques, is primarily indicative of cation disordering, and therefore the formation of antisites, or more appropriately RuTi and TiRu defects [35]. On the other hand, the inset of Fig. 1(b) exhibits the magnetic susceptibility of SrTiO_3 , in which a paramagnetic behavior is observed in the temperature range studied. Such a paramagnetic ground state may be related to both dilute magnetic impurities at the ppm level and oxygen deficiency [36,37].

B. Electrical resistivity

From the temperature dependence of the electrical resistivity data $\rho(T)$ displayed in Fig. 1(c), SrRuO_3 is confirmed to be a ferromagnetic metal, with $d\rho/dT$ being positive in almost all of the temperature range studied. We have also observed a suppression of the spin degree of freedom below the ferromagnetic transition temperature $T_C \approx 160$ K, lowering the electronic scattering probability, a process accompanied by a change in the slope of $\rho(T)$, as indicated by an arrow in Fig. 1(c). On the other hand, the $\rho(T)$ of the insulating compound SrTiO_3 could not be measured due to its high value even at room temperature.

The semiconducting character of the $\text{SrTi}_{0.5}\text{Ru}_{0.5}\text{O}_3$ is clear from the $\rho(T)$ data [Fig. 1(d)], which places this material in the so-called dielectric side of the metal-insulator transition MIT observed along the $\text{SrTi}_{1-x}\text{Ru}_x\text{O}_3$ series. A simple activation process following the Arrhenius law was insufficient to accurately describe the temperature dependence of ρ displayed in the main panel of Fig. 1(d). However, a much better agreement of our $\rho(T > 200$ K) data is achieved by considering a three-dimensional (3D) Mott variable range hopping (VRH) process, with $\rho(T) \propto \rho_0 \exp(T_0/T)^{1/4}$, as evidenced by the inset of Fig. 1(d). This type of process has also been observed in the dielectric side of a MIT in another ruthenium based material $\text{Y}_{2-x}\text{Bi}_x\text{Ru}_2\text{O}_7$ [38].

One description of the Mott VRH model is related to a percolation theory in disordered systems in which some electronic states are accessible to contribute to the total conductivity of the material [39]. The disorder induces localized electronic states which are randomly distributed in position and energy. Treating the partial substitution of Ti by Ru in the SrTiO₃ matrix as a disordered process, localized electronic states at substituted sites may be associated with the emergence of metallic, small regions within the material, richer in Ru concentration, due to composition fluctuations. In our view, these small regions, closely spaced, are interspersed with occasional large regions. Therefore, the ruthenium richer islands embedded into the SrTiO₃ matrix induce hopping conduction among localized electronic states, a feature consistent with the semiconductinglike behavior observed in the SrTi_{0.5}Ru_{0.5}O₃ sample. This description is consistent with the measured spectral weight at the Fermi level, discussed in Sec. IV C 3.

We also mention that a ferromagnetic transition is expected to occur in the Ru-rich regions at temperatures below 160 K. In fact, despite the good agreement of our $\rho(T)$ of SrTi_{0.5}Ru_{0.5}O₃ in the high-temperature range with the VRH model, a subtle deviation from the model is observed to occur in the vicinity of $T^{-1/4} \approx 0.4 \text{ K}^{-1/4}$, as indicated by the continuous red line in the inset of Fig. 1(d). Such a deviation from the VRH model is much more pronounced as temperature is decreased and further indicates a rather complex behavior of $\rho(T)$ in $T < 30 \text{ K}$ temperature range. We also argue that the absence of composition fluctuations in the ruthenium concentration x throughout the material would lead to a better agreement of $\rho(T)$ and the VRH model, as has been observed in Sr₂TiRuO₆ thin films [31].

C. Electronic structure

1. Ground state

We now proceed to the analysis of the electronic structure of the samples by comparing the spectroscopic results with cluster model calculations. Table I displays the parameters used in the double cluster model calculations, which were chosen to give the best agreement with the x-ray spectroscopy measurements. The parameters found are in accordance with previous reported values [28,30]. The reduced values of both the T_σ hybridizations may partly be due to the reduced basis

TABLE I. Parameters used in the double cluster model calculation for SrTi_{0.5}Ru_{0.5}O₃. All values are given in eV.

Parameter	Ti ⁴⁺	Ru ⁴⁺
U	4.2	5.0
Δ	4.5	1.4
T_σ	3.9	1.7
$10Dq$	1.8	4.4
J	0.20	0.75
$pp\sigma - pp\pi$	0.91	0.91
Δ^*		0.6
T^*		0.25

set, as seen in other calculations [28]. Additionally, small differences in the TiO₆ and RuO₆ octahedra, in comparison to the parent compounds, may also affect the T_σ and $10Dq$ parameters.

Table II shows the calculated contributions of the main configurations to the ground state (GS) of SrTi_{0.5}Ru_{0.5}O₃. The configurations are displayed with $d_{\text{Ti}}^{m+r} \underline{L}^{p+r} \underline{C}_{\text{Ru}}^q d_{\text{Ru}}^{n+p+q}$ notation, as well as projected over each TM ion to facilitate comparison with the single cluster results. According to the calculations, most of the GS is dominated by $d^1 \underline{L}^2 d^5$, $d^0 \underline{L} d^5$, $d^1 \underline{L} d^4$, and $d^0 d^4$ configurations. The projected values onto each TM site yielded, for Ti⁴⁺, 45% $d^1 \underline{L}$ + 27% d^0 , and for Ru, 45% $d^5 \underline{L}$ + 26% d^4 . These results are very close to those of single cluster calculations of SrTiO₃ and SrRuO₃ [28,30]. Hence, the most relevant configurations to the GS of SrTi_{0.5}Ru_{0.5}O₃ can be understood as different arrangements of the SrTiO₃ and SrRuO₃ ground states. According to the Δ_{Ti} and U_{Ti} parameters, the Ti⁴⁺ ion should fall close to the frontier of the charge transfer and the intermediate regimes on the Zaanen, Sawatzky, and Allen (ZSA) diagram [40]. However, the high value of the T_σ interaction favors the sharing of an O 2*p* electron, making $d^1 \underline{L}$ the dominant configuration in the ground state of SrTiO₃. On the other hand, the Ru⁴⁺ ion in SrRuO₃ is known to be in a negative charge-transfer regime (NCT) [40], because the lowest energy configuration in the ground state is $d^5 \underline{L}$ and $\Delta_{\text{Ru}}^{\text{eff}} \equiv \Delta_{\text{Ru}} + \epsilon_{\text{multiplets}} < 0$, where $\epsilon_{\text{multiplets}}$ is the energy of the multiplet terms $10Dq_{\text{Ru}}$ and J_{Ru} [30].

In fact, the GS of SrTi_{0.5}Ru_{0.5}O₃ is dominated by the $d^1 \underline{L}^2 d^5$ (21.8%) configuration, which presents one electron transferred from the O 2*p* band to each metal band. This configuration is closely followed by the $d^0 \underline{L} d^5$ (15.3%) and $d^1 \underline{L} d^4$ (14.2%) configurations, while the ionic $d^0 d^4$ configuration contributes with roughly 10%. Projections of these states onto each TM site agree with the single cluster model calculations for SrTiO₃ and SrRuO₃. Hence, it is not a surprise that the GS of SrTi_{0.5}Ru_{0.5}O₃ is well represented by a highly mixed *p-d* character, yielding a mean occupancy in the metal *d* bands of around 5.8 electrons, 0.9 coming from the Ti site and 4.9 from the Ru site. The calculated GS resulted in a magnetic moment of around $1.5 \mu_B$, consistent with the values reported in Sec. IV A. However, since the model is correct up to 10^{-2} eV , as described in Sec. III B, the accurate description of the observed 4% reduction in magnetic moment from SRO to STRO requires a larger basis set than we were able to use here.

TABLE II. Main contributions to the ground-state wave function of SrTi_{0.5}Ru_{0.5}O₃, their projection onto each site, and the mean *d* orbital occupancy.

Ti:Ru		Ti site		Ru site	
Conf.	%	Conf.	%	Conf.	%
$d^1 \underline{L}^2 d^5$	21.8	$d^1 \underline{L}$	45	$d^5 \underline{L}$	45
$d^0 \underline{L} d^5$	15.3	d^0	27	d^4	26
$d^1 \underline{L} d^4$	14.2	$d^2 \underline{L}^2$	23	$d^5 \underline{C}$	13
$d^0 d^4$	9.7	$d^3 \underline{L}^3$	1.3	$d^5 \underline{L} \underline{C}$	2.5
$\langle \hat{n} \rangle \approx 5.8 \text{ elec.}$		$\langle \hat{n} \rangle \approx 0.9 \text{ elec.}$		$\langle \hat{n} \rangle \approx 4.9 \text{ elec.}$	

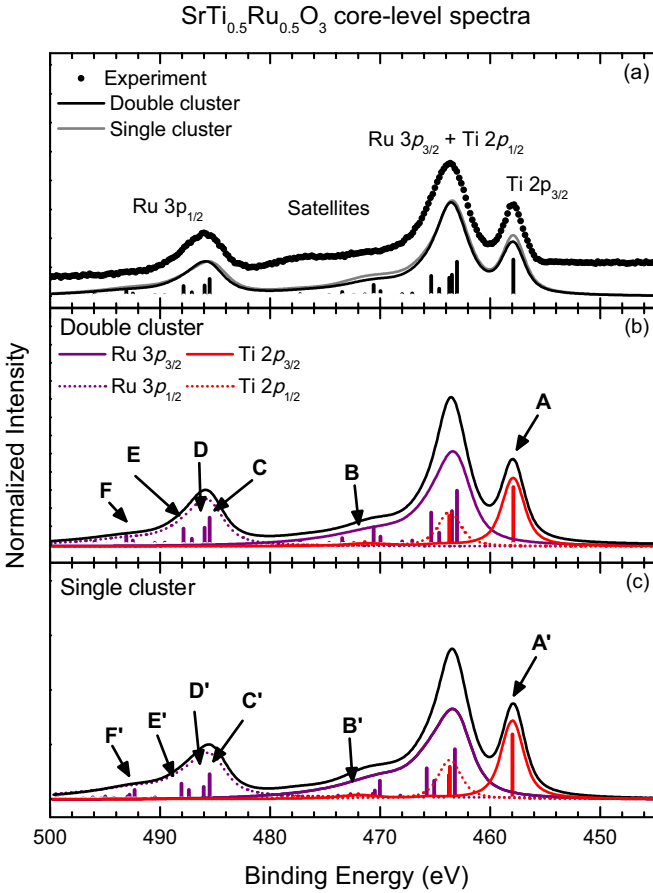


FIG. 2. (a) Ti $2p$ and Ru $3p$ core-level photoemission spectrum of $\text{SrTi}_{0.5}\text{Ru}_{0.5}\text{O}_3$. The spectrum is split, due to spin orbit effects, into the $np_{3/2}$ and $np_{1/2}$ leading structures, which also present satellites. The experimental results are compared to weighted single cluster and double cluster calculations. (b) Projection into the Ru and Ti sites of the core-level spectra calculated with the double cluster. (c) Decomposition of the core-level spectrum calculated with the single cluster. The labels in (b) and (c) refer to relevant discrete final states and their composition is described in Table III.

2. Ti $2p$ and Ru $3p$ core-level spectra

Figure 2(a) depicts the Ti $2p$ and Ru $3p$ core-level photoemission spectrum of $\text{SrTi}_{0.5}\text{Ru}_{0.5}\text{O}_3$. The experimental data display features, split by spin-orbit effects, at the same energies as in the spectra of the pristine SrTiO_3 and SrRuO_3 compounds. Namely, the Ti $2p_{3/2}$ peak appears at 458.2 eV, the Ti $2p_{1/2}$ feature is superimposed with the Ru $3p_{3/2}$ contribution, at around 463.9 eV, whereas the Ru $3p_{3/2}$ component is observed at about 486 eV. Finally, the energy region between 468 and 482 eV presents satellite structures pertaining to the Ti $2p$ and Ru $3p_{3/2}$ main peaks [28,30].

The experimental spectrum in Fig. 2(a) is compared to the cluster model calculation results. The black line represents the core-level spectral weight obtained with the double cluster model, while the gray line is associated with the linear combination of single cluster results for SrTiO_3 and SrRuO_3 [23]. Both calculated curves take into account the different photoionization cross sections of the Ti $2p$ and Ru $3p$ core levels [41]. It is clear that both calculations satisfactorily

TABLE III. Dominant final-state configurations for selected peaks in the core-level spectrum, projected onto their respective site, where \underline{c} represents a core hole. The configurations shown for peaks A (A') and B (B') have similar contributions to their respective final states.

Double cluster		Single cluster	
Peak (site)	Dominant final states	Peak (site)	Dominant final states
A (Ti)	$\underline{cd}^1\underline{L}$, $\underline{cd}^2\underline{L}^2$	A' (Ti)	$\underline{cd}^2\underline{L}^2$, $\underline{cd}^1\underline{L}$
B (Ti)	$\underline{cd}^2\underline{L}^2$, $\underline{cd}^1\underline{L}$	B' (Ti)	$\underline{cd}^2\underline{L}^2$, \underline{cd}^0
C (Ru)	$\underline{cd}^6\underline{LC}$	C' (Ru)	$\underline{cd}^6\underline{LC}$
D (Ru)	$\underline{cd}^6\underline{LC}$	D' (Ru)	$\underline{cd}^6\underline{L}^2$
E (Ru)	$\underline{cd}^6\underline{LC}$	E' (Ru)	$\underline{cd}^6\underline{LC}$
F (Ru)	$\underline{cd}^6\underline{LC}$	F' (Ru)	$\underline{cd}^5\underline{L}$

reproduce the main features of the experimental spectrum, although the many-body configurations contributing to each structure in the spectrum may still differ from one calculation to the other. The decomposition of the calculated core-level spectrum with the double cluster into the Ti $2p_{3/2,1/2}$ (red) and Ru $3p_{3/2,1/2}$ (purple) contributions is shown Fig. 2(b). The labels in the figure indicate final states with different dominant configurations projected in the corresponding ion site, which are displayed in Table III for clarity. The analysis is given in terms of different screening mechanisms, from the ground state to each discrete final state, upon the creation of a TM core hole. Depending on the availability of the screening, final states can be labeled “well-screened,” “poorly screened,” and “unscreened,” and one can also keep track of the nature of the screening (from ligand or coherent bands). The following analysis is performed for the Ti $2p_{3/2}$ and Ru $3p_{1/2}$ parts of the spectra, but they also hold for each respective $np_{1/2}$ part.

The leading structure in Ti $2p_{3/2}$ region of the spectrum (peak A) is mainly composed of the $\underline{cd}^1\underline{L}$ and $\underline{cd}^2\underline{L}^2$ configurations, whereas the satellite (peak B) is dominated by $\underline{cd}^2\underline{L}^2$ and $\underline{cd}^1\underline{L}$ configurations. In turn, in the Ru $3p_{1/2}$ spectrum, the three main peaks and the satellite, labeled C, D, E, and F, are formed by $\underline{cd}^6\underline{LC}$ configurations. For comparison, Fig. 2(c) depicts the single cluster model calculation for the Ti $2p$ (red) and Ru $3p$ (purple) core-level spectral weight. For clarity, the relevant contributions to the labeled peaks are also displayed in Table III. The leading structure in the spectrum (peak A') is composed of the $\underline{cd}^1\underline{L}$ and $\underline{cd}^2\underline{L}^2$ configurations, whereas the satellite (peak B') is ascribed as a sum of two configurations: \underline{cd}^0 and $\underline{cd}^2\underline{L}^2$. On the other hand, the three peaks in the main region of the Ru $3p_{1/2}$ spectrum, labeled C', D', and E', are identified with $\underline{cd}^6\underline{LC}$, $\underline{cd}^6\underline{L}^2$, and $\underline{cd}^6\underline{L}^2$ character, respectively, whereas the structure labeled F' is mainly due to the $\underline{cd}^5\underline{L}$ configuration [30].

The main difference observed in the results of either the single or double cluster models is that the contribution of ligand screened peaks (\underline{L}^2) is reduced in the Ti $2p$ spectrum, and suppressed in the Ru $3p$ core level. The reason for the differences may stem from the fact that both Ti^{4+} and Ru^{4+} ions favor the sharing of an O $2p$ electron, or in other words, the GS of the double perovskite is governed by charge-transfer configurations to such an extent that further ligand screening is not favorable.

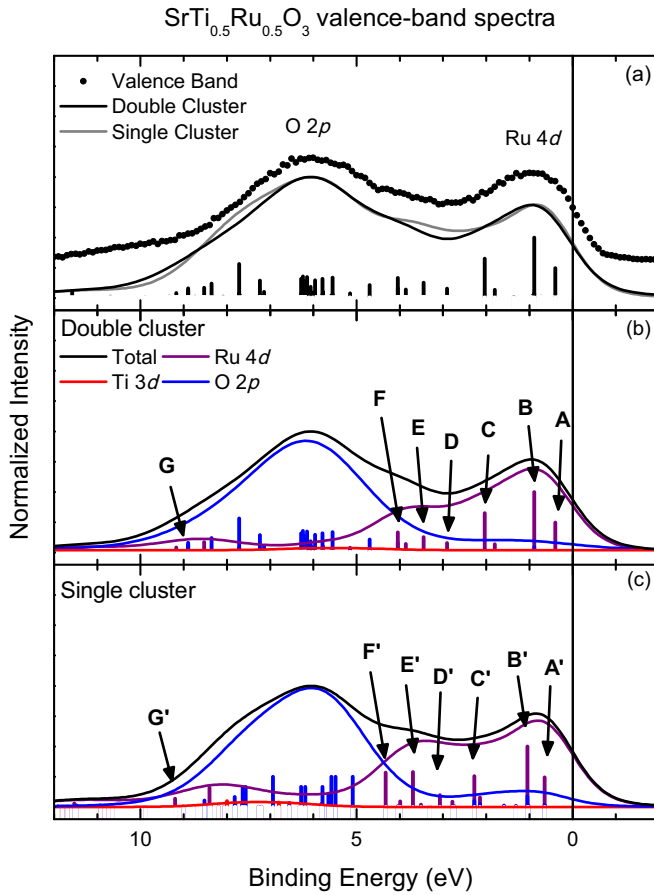


FIG. 3. (a) Valence-band photoemission spectrum of $\text{SrTi}_{0.5}\text{Ru}_{0.5}\text{O}_3$, composed by two main structures related to $\text{O } 2p$ and $\text{Ru } 4d$ occupied states. The experimental results are compared to weighted single cluster and double cluster calculations. (b) Calculated removal state spectra with the double cluster, projected into the Ru and Ti sites. (c) Weighted SrTiO_3 and SrRuO_3 removal state spectra with the single cluster. For (b) and (c), the labels refer to relevant discrete final states and their composition is described in Table IV.

In a recent double cluster model calculation of $\text{Sr}_2\text{FeMoO}_6$ [42], it was shown that the character of the $\text{Fe } 2p$ and $\text{Mo } 3p$ core-level peaks are mostly the same regardless of being calculated with double or single cluster models. In such a system, the Fe^{3+} and Mo^{5+} ions are classified within the charge-transfer ($\Delta < U$) and Mott-Hubbard ($\Delta > U$) regimes, respectively. On the other hand, as shown above, the $\text{Ti } 2p$ and $\text{Ru } 3p$ core levels showed noticeable changes in their character. This may be attributed to the relative importance of TM-O-TM charge fluctuations, which is directly related to the values of U , Δ , and T_σ , and their corresponding classification within the ZSA scheme [40].

3. Valence-band photoemission spectra

Figure 3(a) presents the x-ray valence-band photoemission spectrum of $\text{SrTi}_{0.5}\text{Ru}_{0.5}\text{O}_3$. As noted above, the spectra measured with this photon energy are less surface sensitive than the reported valence-band ultraviolet angle-resolved photoemission spectroscopy spectra on SRO films [43,44]. The

TABLE IV. Dominant final-state configurations, along with projections in the Ru site, for selected peaks in the valence-band spectrum

Peak	Double Cluster		Single Cluster	
	Ti:Ru	Ru site	Peak	final state
A	$d^0\bar{L}d^4 + d^1\bar{L}^2d^4$	$d^4\bar{L}$	A'	$d^5\bar{L}\bar{C}$
B	$d^0\bar{L}d^4 + d^1\bar{L}^2d^4$	$d^4\bar{L}$	B'	$d^5\bar{L}^2$
C	$d^0\bar{L}\bar{C}d^5$	$d^5\bar{L}\bar{C}$	C'	$d^5\bar{L}\bar{C}$
D	$d^0\bar{L}d^4 + d^1\bar{L}^2d^4$	$d^4\bar{L}$	D'	$d^5\bar{L}^2$
E	$d^0\bar{L}d^4 + d^1\bar{L}^2d^4$	$d^4\bar{L}$	E'	$d^5\bar{L}\bar{C}$
F	$d^0\bar{L}^2d^5$	$d^5\bar{L}^2$	F'	$d^5\bar{L}^2$
G	$d^0\bar{L}\bar{C}d^5$	$d^5\bar{L}\bar{C}$	G'	$d^4\bar{L}$

spectrum is composed of the $\text{Ru } 4d$ band region, from 3.0 eV to E_F , and the $\text{O } 2p$ band region, from 10 to 3.0 eV. The overall shape of the spectrum resembles the one from SrRuO_3 [30], particularly because at this photon energy, the $\text{Ru } 4d$ photoionization cross section $\sigma_{\text{Ru } 4d}$ is at least one order of magnitude greater than $\sigma_{\text{Ti } 3d}$ [41]. There are no reports of a high-energy valence-band spectrum for this material, but the obtained spectrum displays features at the same binding energies as other measurements with photons of 22.1 eV [19], 40 eV [18], and 600 eV [22]. Despite the semiconducting character of the sample, the valence-band XPS spectrum shows large spectral weight at the Fermi level, which is consistent with the VRH conductivity reported in Sec. IV B.

The experimental data are compared to the calculated removal ($N - 1$) spectra. The double cluster model is shown by the black solid line, whereas the weighted SrTiO_3 and SrRuO_3 single cluster model calculations appear in the gray line [23]. Both theoretical approaches successfully reproduce the energy positions and relative intensities of the features displayed in the spectrum. In spite of that, each calculated spectrum of STRO is composed of states with different character, which will be shown in what follows.

Figure 3(b) presents the decomposition of the calculated removal spectra from the double cluster model into the partial $\text{Ru } 4d$, $\text{O } 2p$, and $\text{Ti } 3d$ contribution. The dominant configuration of the labeled peaks, projected only into the Ru site, are displayed in Table IV. Again, the analysis is given in terms of the different screening mechanisms, from the ground state to each discrete final state, upon the removal of a TM valence electron. Peaks A, B, D, and E are mainly composed of the $d^0\bar{L}d^4$ and $d^1\bar{L}^2d^4$ final states, which corresponds to a $d^4\bar{L}$ state in the Ru site. After the ejection of the photoelectron, leaving the system with $N - 1$ electrons, these configurations can be achieved via three processes: (i) ligand screening on the Ru site; (ii) ligand screening on the Ti site; but also (iii) the absence of screening, due to the different relevant configurations present in the ground state. Peaks C and G are mainly composed of the $d^0\bar{L}\bar{C}d^5$ final state. Given the calculated GS, this state can be achieved through (i) ligand screening or, (ii) coherent screening. Finally, peak F is mainly composed of the $d^0\bar{L}^2d^5$ final state, which arises from

(i) ligand screening, as well as (ii) absence of screening. For comparison, Fig. 3(c) shows the calculated removal spectra from the weighted single cluster model. The dominant configuration of the peaks presented in the figure is also displayed in Table IV. The results for SRO have been previously addressed elsewhere [30].

It is evident that the character of the peaks displays clear differences when both models are considered. The most remarkable one and related to the characters of the peaks is the reduction and shift to higher binding energies of coherent (C) and ligand screened states ($d^5\bar{L}^2$). The peaks close to E_F are then composed of a mixture of $d^4\bar{L}$ states in $\text{SrTi}_{0.5}\text{Ru}_{0.5}\text{O}_3$, rather than $d^5\bar{L}C$ in SrRuO_3 . Since $\text{O } 2p$ states are involved in the lowest energy charge fluctuation in SrRuO_3 [30,45], we speculate that the change in the character of the states close to the Fermi level may be related to the rise in conductivity despite increasing Ti-Ru disorder, as reported for $\text{Sr}_2\text{TiRuO}_6$ thin films [22].

4. O 1s x-ray absorption spectroscopy

Figure 4(a) displays the O 1s x-ray absorption spectrum of $\text{SrTi}_{0.5}\text{Ru}_{0.5}\text{O}_3$. This technique is related to transitions from O 1s to empty O 2p states. Since O 2p states are covalently mixed with Ti and Ru bands (and also with Sr bands), transitions to these states provide information on the unoccupied TM bands. The experimental data resemble a linear combination of both SrTiO_3 [46] and SrRuO_3 [30] O 1s XAS spectra and shows the first Ru and Ti features at 529.2 and 531 eV, respectively, followed by a plateau at 532.3 eV and a peak at 533.6 eV. Finally, the Sr 4d states appear between 537.0 and 540 eV. The Ti 3d and Ru 4d derived regions of the experimental spectrum are compared to the O 2p character of the calculated addition ($N + 1$) spectrum for the double cluster calculation, shown by the black solid line, and the sum of the two single cluster model calculations for SrTiO_3 and SrRuO_3 , shown by the gray dotted line [23]. Both spectral shapes are similar and reproduce with good accuracy the intensities and energy positions of the features in the spectrum.

Similar to the analysis performed for the XPS spectra, we explore the composition of the different final states in the XAS spectra. Figure 4(b) shows the decomposition of the calculated O 2p addition spectrum for $\text{SrTi}_{0.5}\text{Ru}_{0.5}\text{O}_3$ with the double cluster model. The total spectral weight is split into Ti and Ru partial contributions, and the labels indicate the dominant configuration and the corresponding multiplet of each final state. In the Ti part of the spectrum, shown in red, the two main peaks at 531.0 and 533.5 eV are due to the addition of an electron in the Ti 3d t_{2g} and Ti 3d e_g orbitals, respectively. The energy separation of the two peaks is around 2.5 eV, consistent with the $10Dq_{\text{Ti}}$ value of 1.5 eV. In turn, the Ru component of the spectrum, shown in purple, presents three main peaks. The first peak at 529.2 eV is due to the addition of a minority Ru 4d t_{2g} electron, while the other two peaks are due to the addition of a majority (532.2 eV) and minority (536.6 eV) e_g electron, a feature consistent with the splitting of $2J_{\text{Ru}} = 1.5$ eV. The separation of the t_{2g} peak and the center of the e_g peaks is also consistent with the value of $10Dq_{\text{Ru}} \approx 4.3$ eV.

For comparison, Fig. 4(c) shows the single cluster model calculation for SrTiO_3 and SrRuO_3 . According to the labels,

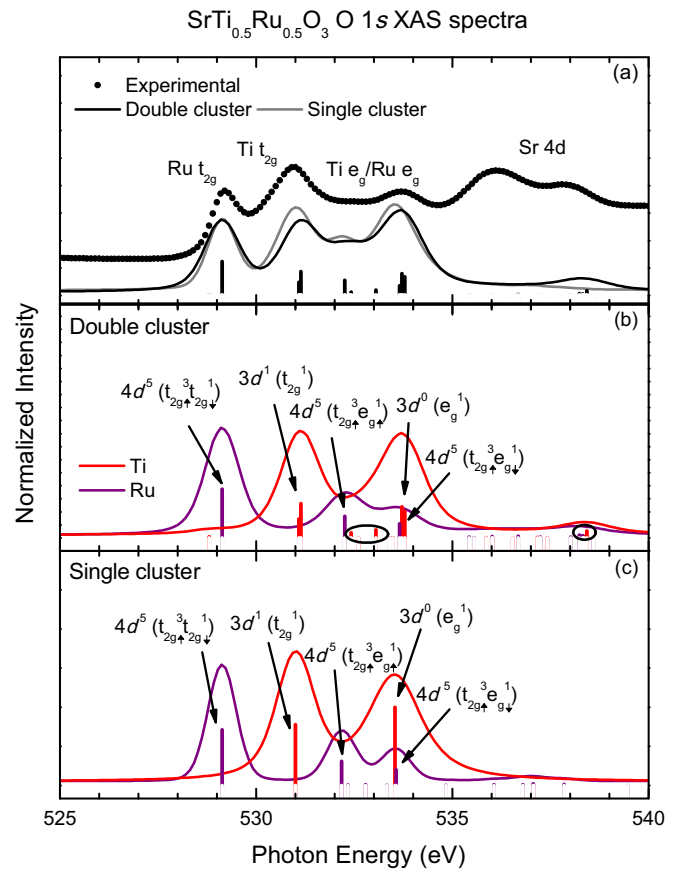


FIG. 4. (a) O 1s x-ray absorption spectrum of $\text{SrTi}_{0.5}\text{Ru}_{0.5}\text{O}_3$. The labels refer to the metal bands which are covalently mixed with the unoccupied O 2p states. The experimental results are compared to double cluster and weighted single cluster calculations. (b) Calculated O 2p addition spectra with the double cluster, projected into the Ru and Ti sites. Circles point to extra structures in the spectrum when the Ti-Ru interaction is included. (c) Calculated O 2p addition spectra with weighted SrTiO_3 and SrRuO_3 single cluster calculations. In (b) and (c), the labels refer to the dominant configuration (multiplet) in the relevant discrete final states.

the Ti 3d features located at 531 and 533.5 eV correspond to transitions to $3d^1t_{2g}$ and $3d^1e_g$ states, respectively. The Ru 4d peaks at 529.2 eV correspond to transitions to minority $4d^5t_{2g}$ states. The other two peaks at 532.2 and 533.6 eV are due to majority and minority $4d^5e_g$ states, respectively.

It is clear that, in the case of O 1s XAS of $\text{SrTi}_{0.5}\text{Ru}_{0.5}\text{O}_3$, the spectrum resembles very closely, not only in shape, but also in the composition of the significant final states, the sum of the spectra of the SrTiO_3 and SrRuO_3 samples. Nevertheless, it is worth noting that there are some small differences in the final states with Ti contribution close to 533 eV and in the intensity of satellites at about 539 eV, as highlighted in Fig. 4(b), even though they are not relevant for the XAS technique.

5. Screening mechanisms and the Ti-Ru octahedra interaction

After analyzing the results described above, there are three main aspects we intend to discuss regarding the different

character of the electronic structure of $\text{SrTi}_{0.5}\text{Ru}_{0.5}\text{O}_3$ when the Ru-Ti interaction is explicitly included.

First, the manifestation of the Ti-Ru interaction clearly depends on the experimental technique used. Indeed, the O 2*p* addition spectra calculated with both approaches—single and double cluster—were able reproduce the O 1*s* XAS spectra of this system, assigning almost identical character for each peak in the spectra, indicating that the inclusion of this interaction is not relevant to the description of the experimental data. On the other hand, the character of the structures in core-level and valence-band photoemission spectra is quite different when calculated with single or double cluster approaches. In these cases, the Ti-Ru interaction appears to be relevant and the main difference emerges from the availability of screening mechanisms in each case.

Second, whenever the inclusion of this interaction yielded differences in the screening mechanisms, changes in their expected energy positions were not realized. In (negative) charge-transfer materials, it is expected that leading structures would display screened character, whereas satellite features would show unscreened/poorly screened character [40]. In other words, the screening of the photoelectron would be favorable, and the low-energy features in the electronic structure of charge-transfer materials would have mixed character. This is an important result for better understanding of the character and microscopic origin of low-energy transitions in TM compounds [3,40]. Then, the differences obtained in the core-level and valence-band photoemission spectra of $\text{SrTi}_{0.5}\text{Ru}_{0.5}\text{O}_3$ with the double cluster calculation lead to a different interpretation of its electronic structure.

Finally, the other important aspect is the fact that TM compounds usually show similar trends in both core-level and valence-band spectra. Namely, both techniques would share the same type of screening mechanisms [30,47–50]. This is not what happens in $\text{SrTi}_{0.5}\text{Ru}_{0.5}\text{O}_3$ when calculated with the double cluster model. According to our calculations, upon removal of a Ru 4*d* electron, unscreened and screened states in the Ti site may contribute to the low-energy region of the spectrum, along with the usual screening in the Ru site. On the other hand, each core-level spectrum is composed of states where the screening takes place only in the respective site. In other words, the valence-band spectrum shows a coupling of the different octahedra, while the core-level spectra show no sign of coupling. It is important to notice that only the explicit inclusion of the Ti-Ru interaction is capable of capturing these features. As a comparison, a different behavior of the screening mechanisms in the core-level and valence-band spectra was also observed in a double cluster model study on $\text{Sr}_2\text{FeMoO}_6$. While in the valence-band spectrum there is a clear signature of Fe-Mo nonlocal screening, the character of

the Fe 2*p* and Mo 3*p* core-level peaks is similar to the ones obtained by single cluster model calculations [42], indicating that the interplay between two different TMO_6 octahedra depend on the ZSA [40] classification of each system.

V. SUMMARY AND CONCLUSIONS

We have studied the results of magnetization and electrical resistivity measurements, as well as studied the electronic structure of SrTiO_3 , $\text{SrTi}_{0.5}\text{Ru}_{0.5}\text{O}_3$, and SrRuO_3 polycrystals with x-ray photoemission and absorption spectroscopies. The spectroscopic results were interpreted by using single and double cluster models. The $M(T)$ data for $\text{SrTi}_{0.5}\text{Ru}_{0.5}\text{O}_3$ reveal a deviation of the Curie-Weiss behavior just below 160 K, which is consistent with the occurrence of *RuTi* and *TiRu* defects. The behavior of the $\rho(T)$ data measured for $\text{SrTi}_{0.5}\text{Ru}_{0.5}\text{O}_3$ agrees well with a 3D Mott variable range hopping process, consistent with the emergence of small metallic regions richer in Ru concentration due to composition fluctuations. This feature is supported by the finite spectral weight at the Fermi level seen in the valence-band XPS spectrum. The core-level, valence-band, and O 1*s* spectra of $\text{SrTi}_{0.5}\text{Ru}_{0.5}\text{O}_3$ were simulated with a double cluster (DC) and by properly weighing the SrTiO_3 and SrRuO_3 single cluster calculations (SC). The experimental results for $\text{SrTi}_{0.5}\text{Ru}_{0.5}\text{O}_3$ were found to be correctly reproduced, in terms of relative intensities and energy position of the different features, with both the DC and SC approaches. However, the character of the peaks in the spectra yielded different results, depending on the theoretical model and on the experimental technique simulated. While the assignments in the O 1*s* XAS spectra are pretty much independent of the explicit inclusion of Ti-Ru interaction, the character of the core-level and valence-band photoemission spectral features were clearly modified by this interaction. Our results indicate that both Ti-Ru disorder and electronic correlation are important ingredients for the description of the electronic structure of the $\text{SrTi}_{1-x}\text{Ru}_x\text{O}_3$ series close to $\approx 50\%$ substitution.

ACKNOWLEDGMENTS

This work was supported by Brazil's agencies FAPESP (Grants No. 2013/07296-2, No. 2014/12401-2, and No. 2014/19245-6), CAPES, and CNPq (Grants No. 6444712/2014-3, No. 306006/2015-4, and No. 307153/2016-9). We acknowledge PGM and SXS beamlines staff for technical support and the CNPEM/LNLS for granting beam time under Projects No. SXS-17731 and No. PGM-17732.

-
- [1] J. G. Bednorz and K. A. Müller, *Z. Phys. B* **64**, 189 (1986).
 [2] M. N. Baibich, J. M. Broto, A. Fert, F. Nguyen Van Dau, F. Petroff, P. Etienne, G. Creuzet, A. Friederich, and J. Chazelas, *Phys. Rev. Lett.* **61**, 2472 (1988).

- [3] M. Imada, A. Fujimori, and Y. Tokura, *Rev. Mod. Phys.* **70**, 1039 (1998).
 [4] Y. Maeno, H. Hashimoto, K. Yoshida, S. Nishizaki, T. Fujita, J. G. Bednorz, and F. Lichtenberg, *Nature (London)* **372**, 532 (1981).

- [5] C. B. Eom, R. J. Cava, R. M. Fleming, J. M. Phillips, R. B. vanDover, J. H. Marshall, J. W. P. Hsu, J. J. Krajewski, and W. F. Peck, *Science* **258**, 1766 (1992).
- [6] G. Cao, S. McCall, M. Shepard, J. E. Crow, and R. P. Guertin, *Phys. Rev. B* **56**, 321 (1997).
- [7] H. Shaked, J. Jorgensen, O. Chmaissem, S. Ikeda, and Y. Maeno, *J. Solid State Chem.* **154**, 361 (2000).
- [8] M. K. Crawford, R. L. Harlow, W. Marshall, Z. Li, G. Cao, R. L. Lindstrom, Q. Huang, and J. W. Lynn, *Phys. Rev. B* **65**, 214412 (2002).
- [9] F. W. Lytle, *J. Appl. Phys.* **35**, 2212 (1964).
- [10] K. van Benthem, C. Elsässer, and R. H. French, *J. Appl. Phys.* **90**, 6156 (2001).
- [11] H. Kobayashi, M. Nagata, R. Kanno, and Y. Kawamoto, *Mater. Res. Bull.* **29**, 1271 (1994).
- [12] P. B. Allen, H. Berger, O. Chauvet, L. Forro, T. Jarlborg, A. Junod, B. Revaz, and G. Santi, *Phys. Rev. B* **53**, 4393 (1996).
- [13] A. P. Mackenzie, J. W. Reiner, A. W. Tyler, L. M. Galvin, S. R. Julian, M. R. Beasley, T. H. Geballe, and A. Kapitulnik, *Phys. Rev. B* **58**, R13318(R) (1998).
- [14] P. Kostic, Y. Okada, N. C. Collins, Z. Schlesinger, J. W. Reiner, L. Klein, A. Kapitulnik, T. H. Geballe, and M. R. Beasley, *Phys. Rev. Lett.* **81**, 2498 (1998).
- [15] L. Klein, J. S. Dodge, C. H. Ahn, G. J. Snyder, T. H. Geballe, M. R. Beasley, and A. Kapitulnik, *Phys. Rev. Lett.* **77**, 2774 (1996).
- [16] A. Callaghan, C. W. Moeller, and R. Ward, *Inorg. Chem.* **5**, 1572 (1966).
- [17] J. M. Longo, P. M. Raccach, and J. B. Goodenough, *J. Appl. Phys.* **39**, 1327 (1968).
- [18] M. Abbate, J. A. Guevara, S. L. Cuffini, Y. P. Mascarenhas, and E. Morikawa, *Eur. Phys. J. B* **25**, 203 (2002).
- [19] J. Kim, J.-Y. Kim, B.-G. Park, and S.-J. Oh, *Phys. Rev. B* **73**, 235109 (2006).
- [20] P.-A. Lin, H.-T. Jeng, and C.-S. Hsue, *Phys. Rev. B* **77**, 085118 (2008).
- [21] K. Maiti, *Phys. Rev. B* **77**, 212407 (2008).
- [22] K. Nogami, K. Yoshimatsu, H. Mashiko, E. Sakai, H. Kumigashira, O. Sakata, T. Oshima, and A. Ohtomo, *Appl. Phys. Express* **6**, 105502 (2013).
- [23] See Supplemental Material at <http://link.aps.org/supplemental/10.1103/PhysRevB.100.075132> for details on sample preparation, x-ray powder diffraction, x-ray spectroscopy, and cluster model calculations of the end members.
- [24] M. Abbate, F. Vicentin, V. Compagnon-Cailhol, M. Rocha, and H. Tolentino, *J. Synchrotron Radiat.* **6**, 964 (1999).
- [25] S. Tanuma, C. J. Powell, and D. R. Penn, *Surf. Interface Anal.* **43**, 689 (2011).
- [26] G. van der Laan, C. Westra, C. Haas, and G. A. Sawatzky, *Phys. Rev. B* **23**, 4369 (1981).
- [27] J. C. Slater and G. F. Koster, *Phys. Rev.* **94**, 1498 (1954).
- [28] A. E. Bocquet, T. Mizokawa, K. Morikawa, A. Fujimori, S. R. Barman, K. Maiti, D. D. Sarma, Y. Tokura, and M. Onoda, *Phys. Rev. B* **53**, 1161 (1996).
- [29] M. Taguchi, A. Chainani, N. Kamakura, K. Horiba, Y. Takata, M. Yabashi, K. Tamasaku, Y. Nishino, D. Miwa, T. Ishikawa, S. Shin, E. Ikenaga, T. Yokoya, K. Kobayashi, T. Mochiku, K. Hirata, and K. Motoya, *Phys. Rev. B* **71**, 155102 (2005).
- [30] E. B. Guedes, M. Abbate, K. Ishigami, A. Fujimori, K. Yoshimatsu, H. Kumigashira, M. Oshima, F. C. Vicentin, P. T. Fonseca, and R. J. O. Mossaneck, *Phys. Rev. B* **86**, 235127 (2012).
- [31] K. W. Kim, J. S. Lee, T. W. Noh, S. R. Lee, and K. Char, *Phys. Rev. B* **71**, 125104 (2005).
- [32] R. J. Green, M. W. Haverkort, and G. A. Sawatzky, *Phys. Rev. B* **94**, 195127 (2016).
- [33] W. Tong, F.-Q. Huang, and I.-W. Chen, *J. Phys.: Condens. Matter* **23**, 086005 (2011).
- [34] B. Dalal, B. Sarkar, and S. De, *J. Alloys Compd.* **667**, 248 (2016).
- [35] J. A. Rodgers, A. J. Williams, M. J. Martinez-Lope, J. A. Alonso, and J. P. Attfield, *Chem. Mater.* **20**, 4797 (2008).
- [36] A. Lopez-Bezanilla, P. Ganesh, and P. B. Littlewood, *Phys. Rev. B* **92**, 115112 (2015).
- [37] J. M. D. Coey, M. Venkatesan, and P. Stamenov, *J. Phys.: Condens. Matter* **28**, 485001 (2016).
- [38] S. Yoshii and M. Sato, *J. Phys. Soc. Jpn.* **68**, 3034 (1999).
- [39] V. Ambegaokar, B. Halperin, and J. Langer, *J. Non-Cryst. Solids* **8-10**, 492 (1972).
- [40] J. Zaanen, G. A. Sawatzky, and J. W. Allen, *Phys. Rev. Lett.* **55**, 418 (1985).
- [41] J. J. Yeh and I. Lindau, *At. Data Nucl. Data Tables* **32**, 1 (1985).
- [42] H. P. Martins, E. B. Guedes, R. J. O. Mossaneck, F. D. Prado, A. Caneiro, and M. Abbate, *RSC Adv.* **8**, 3928 (2018).
- [43] D. E. Shai, C. Adamo, D. W. Shen, C. M. Brooks, J. W. Harter, E. J. Monkman, B. Burganov, D. G. Schlom, and K. M. Shen, *Phys. Rev. Lett.* **110**, 087004 (2013).
- [44] H. F. Yang, Z. T. Liu, C. C. Fan, Q. Yao, P. Xiang, K. L. Zhang, M. Y. Li, H. Li, J. S. Liu, D. W. Shen, and M. H. Jiang, *Phys. Rev. B* **93**, 121102(R) (2016).
- [45] T. Mizokawa, H. Namatame, A. Fujimori, K. Akeyama, H. Kondoh, H. Kuroda, and N. Kosugi, *Phys. Rev. Lett.* **67**, 1638 (1991).
- [46] L. Soriano, M. Abbate, A. Fernández, A. R. González-Elipe, and J. M. Sanz, *Surf. Interface Anal.* **25**, 804 (1997).
- [47] H.-D. Kim, H.-J. Noh, K. H. Kim, and S.-J. Oh, *Phys. Rev. Lett.* **93**, 126404 (2004).
- [48] R. J. O. Mossaneck, M. Abbate, T. Yoshida, A. Fujimori, Y. Yoshida, N. Shirakawa, H. Eisaki, S. Kohnno, and F. C. Vicentin, *Phys. Rev. B* **78**, 075103 (2008).
- [49] R. Eguchi, M. Taguchi, M. Matsunami, K. Horiba, K. Yamamoto, Y. Ishida, A. Chainani, Y. Takata, M. Yabashi, D. Miwa, Y. Nishino, K. Tamasaku, T. Ishikawa, Y. Senba, H. Ohashi, Y. Muraoka, Z. Hiroi, and S. Shin, *Phys. Rev. B* **78**, 075115 (2008).
- [50] R. J. O. Mossaneck and M. Abbate, *J. Phys.: Condens. Matter* **22**, 375602 (2010).